Supplementary Information

Utilizing hydrogen evolution reaction: bio-inspired pH-sensitive electrolyte for ultra-stable zinc-ion batteries at high temperatures

Fan Bu[1,2,‡], Qiwen Wu[1,2,‡], Jingzhu Chen[1,2,‡], Wenbo Zhao[1,2], Yong Gao[3,1], Jipeng Chen[1,2], Ting Zhang[1,2], Yu Zhang[1], Salah A. Makhlouf[4], Cao Guan[1,2]*

[1]Institute of Flexible Electronics, Northwestern Polytechnical University, Xi'an 710072, China.

[2]Key laboratory of Flexible Electronics of Zhejiang Province, Ningbo Institute of Northwestern Polytechnical University, Ningbo 315103, China.

[3]School of Chemistry, Dalian University of Technology, Dalian 116024, China.

[4]Physics Department, Faculty of Science, Assiut University, Assiut 71516, Egypt.

[‡]These authors contribute equally: Fan Bu, Qiwen Wu, Jingzhu Chen.

Corresponding Authors

*Email: iamcguan@nwpu.edu.cn (C. Guan)

Table of Contents

Experimental Methods

Material synthesis

The ammonium zirconium hexafluoride/$Zn(OTf)_2$ (AZH/$Zn(OTf)_2$) electrolytes were constructed by adding different concentrations (0.1 M, 0.3 M and 0.5 M) of AZH into 2 M $Zn(OTf)_2$ solution. The $Na_2V_6O_{16}\cdot 1.63H_2O$ (NVO) nanowires were synthesized via a previously reported hydrothermal method[1]. Specifically, 8 mmol (1.46 g) V_2O_5 was added into 170 mL deionized (DI) water, and mixed with 8 mmol NaOH (0.32 g). After stirring at 800 rpm in a magnetic mixer for 4 hours, the mixed yellow solution was moved to a Teflon-lined stainless steel autoclave, and then heated in an electric oven at 180 °C for 24 hours. After cooling down to room temperature, the sample was thoroughly washed with ethyl alcohol and DI water. Finally, the sample was dried for 24 hours in a vacuum chamber at 60 ° C and pulverized into powder.

The non-pH-triggered ZrO_2/ZnF_2 (NPT@Zn) electrode was prepared by a blade coating method. First, ZrO_2/ZnF_2 powder, super P and polyvinylidene fluoride (PVDF) were mixed in a weight ratio of 8:1:1. The mixture was dispersed in N-methyl-2-pyrrolidone (NMP) and stirred for 24 hours to form a homogeneous slurry. The slurry was then coated onto a polished Zn foil (10 μm) with a controlled thickness of 50 μm. Finally, the Zn foil was dried for 12 hours in a vacuum chamber at 80 °C, resulting in the NPT@Zn control electrode. This coating method ensures the formation of a ZrO_2/ZnF_2 layer without any pH-triggered reactions.

Characterization

Raman spectra were conducted using a confocal Raman system (WITec Alpha300R) equipped with an optical microscope (Nikon). Contact angles were measured by DSA25 (KRUSS). In situ optical observations were studied via a microscope (ECLIPSE LV150N, Nikon). X-ray photoelectron spectroscopy (XPS) studies were revealed via Kratos (Axis Supra). Time-of-flight secondary-ion mass spectrometry (TOF-SIMS) and focused ion beam-scanning electron microscope (FIB-SEM) were performed via multi-functional focused ion beam electron microscope (FIB, all-in-one system). The morphologies were obtained from field emission scanning electron microscope (Zeiss Gemini SEM 300, 0.02-30.0 kV) and high resolution transmission electron microscope (Talos F200X, FEI). Crystal structures were characterized by X-ray diffraction (Bruker D8 Advance) using Cu Kα radiation. The ^{2}H nuclear magnetic resonance (NMR) spectra were revealed via ADVANCE NEO 500 (Bruker) spectrometer. Fourier transform infrared spectroscopy (FTIR) spectra were recorded on Tensor II (Bruker) with a resolution of 0.4 cm^{-1}.

Online electrochemical mass spectroscopy measurements

The online electrochemical mass spectroscopy (OEMS) measurement was conducted on a PrismaPro differential electrochemical mass spectrometer (PFEIFFER) connected to an electrochemical workstation (CHI 660E). High purity argon gas is passed through the components to remove air and ensure no air leaks before electrochemical tests. During the operation of batteries, the evolved hydrogen gas in the space is carried by the argon and analyzed in the mass spectrometer. The battery devices are placed in an oven to ensure they are always in a high-temperature environment (80 °C). Ti foils are

placed between the electrodes and steel cell components to reduce side reactions between the aqueous electrolyte and steel parts.

Electrochemical measurements

Electrochemical measurements were conducted using Zn electrodes with different thicknesses. 10 μm Zn plate (7.14 mg cm^{-2}, 5.85 mAh cm^{-2}) was used in most experiments and tests. 20 μm Zn plate (14.3 mg cm^{-2}, 11.7 mAh cm^{-2}) was used for the Zn//Zn cell cycled at 85.5% depth of discharge (DOD) under 20 °C. Zn//Cu and Zn//Zn cells were prepared by CR-2025 type coin cells with AZH/$Zn(OTf)_2$ (0.3/2 M) electrolytes to evaluate the Coulombic efficiency (CE) and cycling performance. The current densities were set ranging from 2 to 20 mA cm^{-2} for Zn//Zn cells. The corrosion and hydrogen evolution reaction (HER) behavior of Zn electrodes were measured by linear scanning voltammetry at a scan rate of 5 mV s^{-1}. Full cells were assembled using NVO as the cathode, Zn foil as the anode and AZH/$Zn(OTf)_2$ as the electrolyte. The voltage range was set as 0.2-1.6 V under different current densities (0.2-5 A g^{-1}). The cathode was composed of polyvinylidene fluoride (PVDF), super P and NVO in a 1:1:8 weight ratio. For the high mass loading Zn-ion batteries (ZIBs) and pouch cells, the cathode was composed of PVDF, super P and V_2O_5 in a 1.2:1.5:7.5 weight ratio. The energy density of ZIBs was calculated according to the whole mass of both electrodes. Cyclic voltammetry (CV) and galvanostatic charge/discharge (GCD) curves were conducted on the electrochemical workstation (CHI760E). Rate and long cycling performance were measured by the battery test system (LAND CT3002A5V). All the controlled cells were tested under the same conditions.

The calculation formulas for the used electrochemical parameters are provided. The DOD is explicitly defined as the following equation:

$$DOD = \frac{C_{Zn,reactive}}{C_{Zn,overall}} \times 100\%$$

where $C_{Zn,reactive}$ is the capacity involved in the electrode reaction and $C_{Zn,overall}$ is the overall capacity of the Zn metal anode.

The energy density of full ZIB is calculated by the following equation:

$$E = \frac{\int IUdt}{m}$$

where *E* is the energy density, *I* is the discharging current, *dt* represents the time differential and *m* refers to the whole mass of both active electrodes (excluding the current collector).

Computational simulations

The geometric optimizations based on density functional theory (DFT) was carried out using the Vienna Ab initio Simulation Package (VASP)[2]. The generalized gradient approximation (GGA) of Perdew-Burke-Ernzerhof (PBE) was used to handle the electronic exchange related functions[3]. Grimme's DFD-D3 method was used to represent the van der Waals interactions[4]. Kinetic energy cutoff was set as 400 eV, and gamma point was used for the Brillouin zone sampling. The energy convergence was 10^{-5} eV and the convergence criterion used for the residual force was 0.02 eV $Å^{-1}$. In all calculation system, a 15 Å vacuum is introduced in the Z-axis direction of structures to avoid interaction between periodic models. Differential charge density and structural analysis were conducted using Vaspkit and VESTA[5].

The adsorption energy ($E_{adsorption}$) between Zn and different substrates is defined as the following equation:

$$E_{adsorption} = E_{substrate+molecule} - E_{substrate} - E_{molecule}$$

where $E_{substrate+molecule}$, $E_{substrate}$ and $E_{molecule}$ are the total energy of the adsorption system, the substrate energy and the energy of the adsorbed molecule, respectively.

In ab initio molecular dynamics (AIMD) simulations, the Nosé-Hoover thermostat for canonical (NVT) ensemble is applied with a time step of 1 fs and a temperature of 353.15 K[6,7].

Ionic and thermal field simulations

An ideal model coupling the current and dilute matter transfer physical fields with COMSOL software was developed to account for the electrode electric field distribution and interfacial ion fluxes. The Zn metal anode surface exhibited a different surface roughness and dimensions (1*1 μm²). The Zn model shapes were constructed based on the results of AFM experiments. Accordingly, it takes 72 s to change the electric field distribution of the models. The initial concentration boundary condition was set to 2 M. In addition, the potential of 0.5 V was used as an energizing voltage between electrode and electrolyte. This roughness was implemented by using Gaussian random.

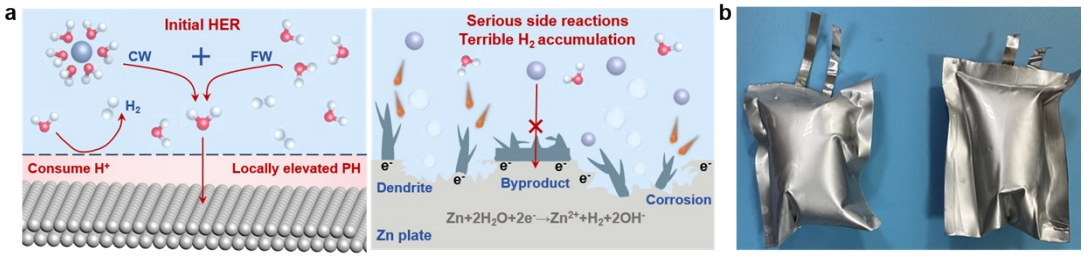

Fig. S1 (a) The interfacial models of Zn anode in pure $Zn(OTf)_2$ electrolyte. (b) The optical image of pouch cells with tremendous H_2 in pure $Zn(OTf)_2$ electrolyte.

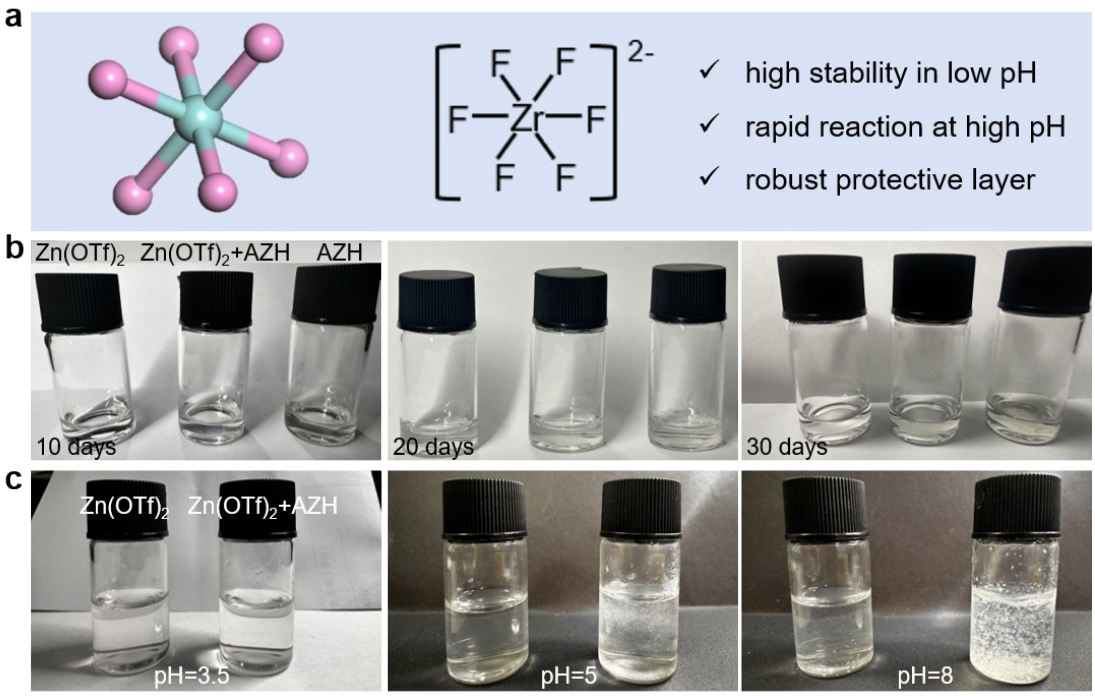

Fig. S2 (a) Molecular formula and structure of $[ZrF_6]^{2-}$ in ammonium zirconium hexafluoride (AZH) molecule. (b) Optical images of different electrolytes after left for 30 days. (c) Optical images of pure $Zn(OTf)_2$ and AZH/$Zn(OTf)_2$ electrolytes at different pH environments.

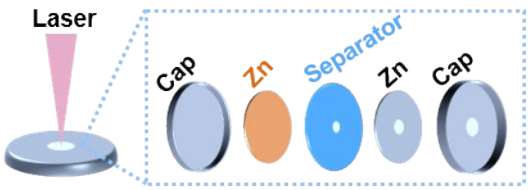

Fig. S3 Schematic diagram of the in situ Raman test setup.

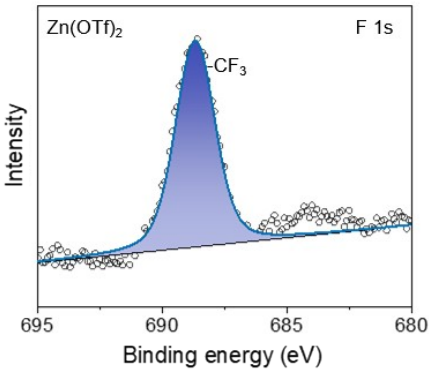

Fig. S4 X-ray photoelectron spectroscopy (XPS) spectra of F 1s for Zn anode cycled in pure $Zn(OTf)_2$ electrolyte.

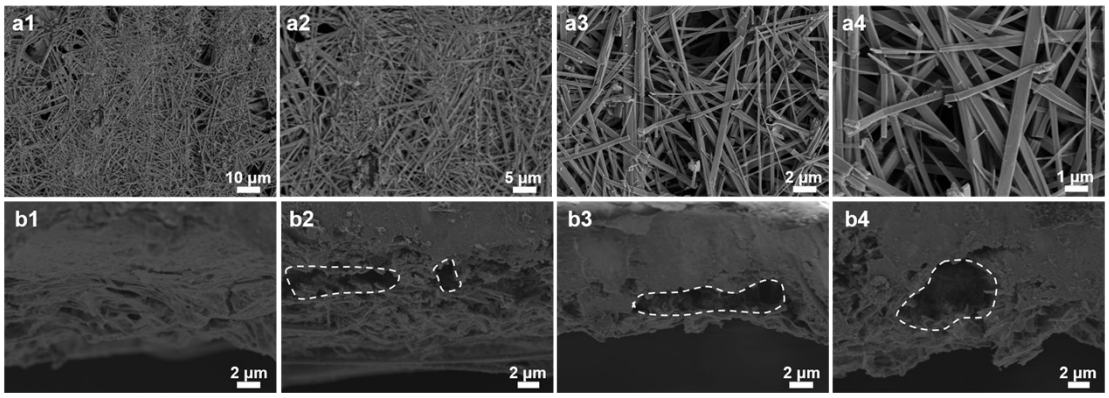

Fig. S5 (a) The scanning electron microscope (SEM) images of the unique porous solid electrolyte interface (SEI) layer composed of interconnected wires. (b) SEM images of Zn electrodes under different Zn utilization conditions in AZH/$Zn(OTf)_2$ electrolyte.

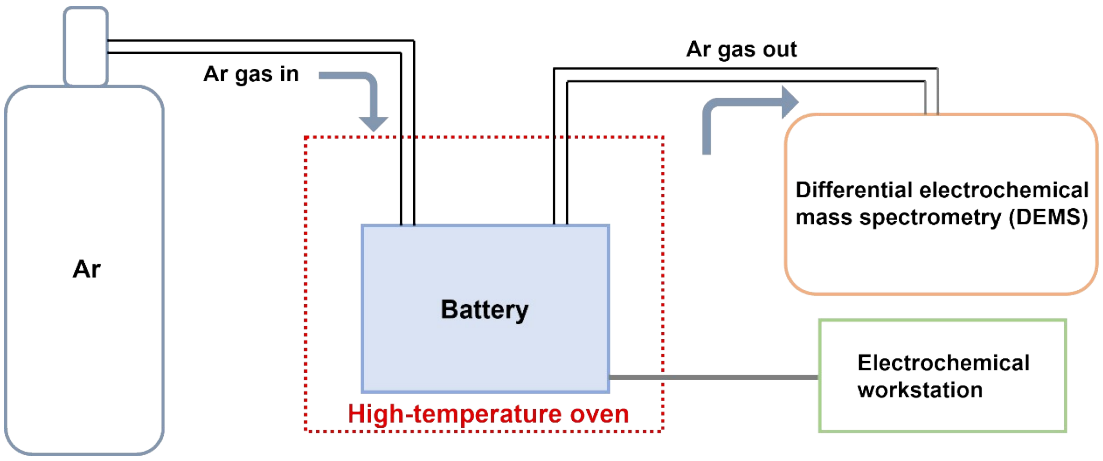

Fig. S6 The schematic diagram of OEMS measurement at high temperatures.

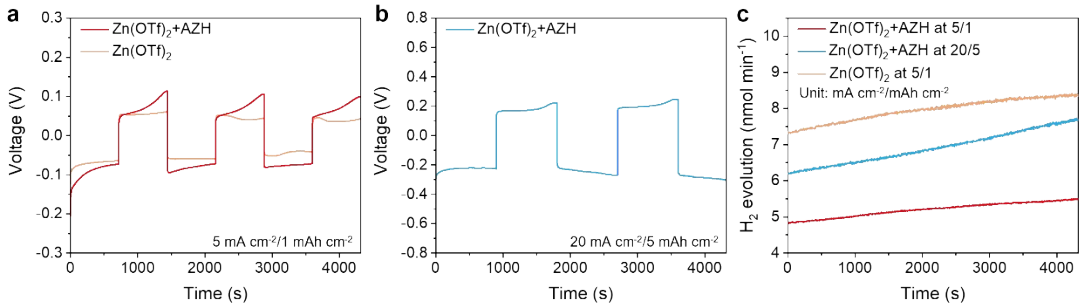

Fig. S7 Voltage profiles of Zn symmetric cells at (a) 5 mA cm^{-2}/1 mAh cm^{-2} and (b) 20 mA cm^{-2}/5 mAh cm^{-2} during OEMS tests. (c) OEMS curves of released hydrogen gas from Zn symmetric cells with different electrolytes.

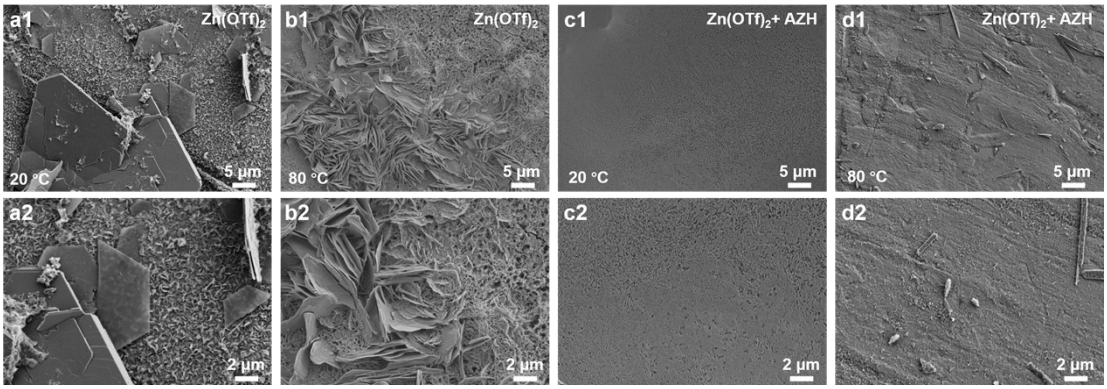

Fig. S8 The SEM images of Zn electrodes after immersed in pure $Zn(OTf)_2$ electrolyte at (a) 20 °C and (b) 80 °C for 7 days. The SEM images of Zn electrodes after immersed in AZH/$Zn(OTf)_2$ electrolyte at (c) 20 °C and (d) 80 °C for 7 days.

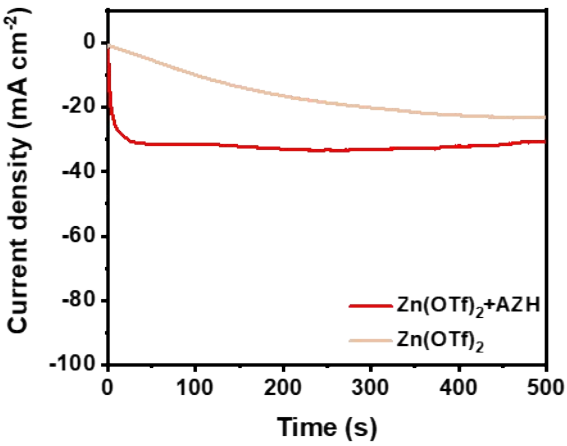

Fig. S9 Chronoamperometry (CA) curves of Zn electrodes in different electrolytes at 80 °C.

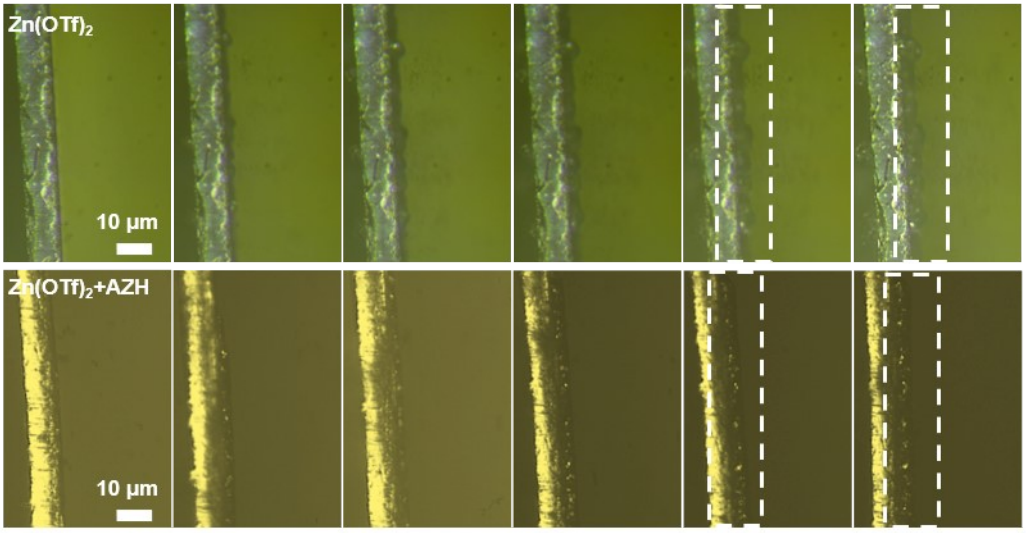

Fig. S10 In situ optical observations of Zn electrodes in pure $Zn(OTf)_2$ and AZH/$Zn(OTf)_2$ electrolytes in symmetric transparent cells.

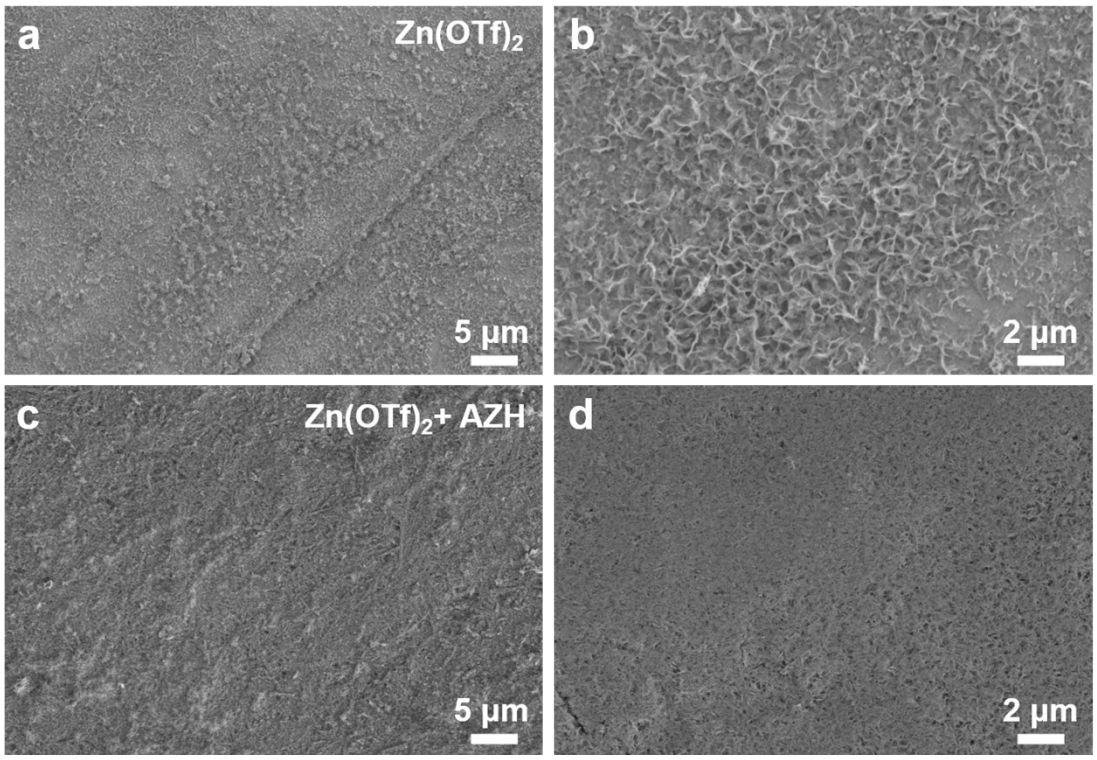

Fig. S11 SEM images of Zn electrodes after deposition for 5 mAh cm^{-2} in (a, b) pure $Zn(OTf)_2$ and (c, d) AZH/$Zn(OTf)_2$ electrolytes.

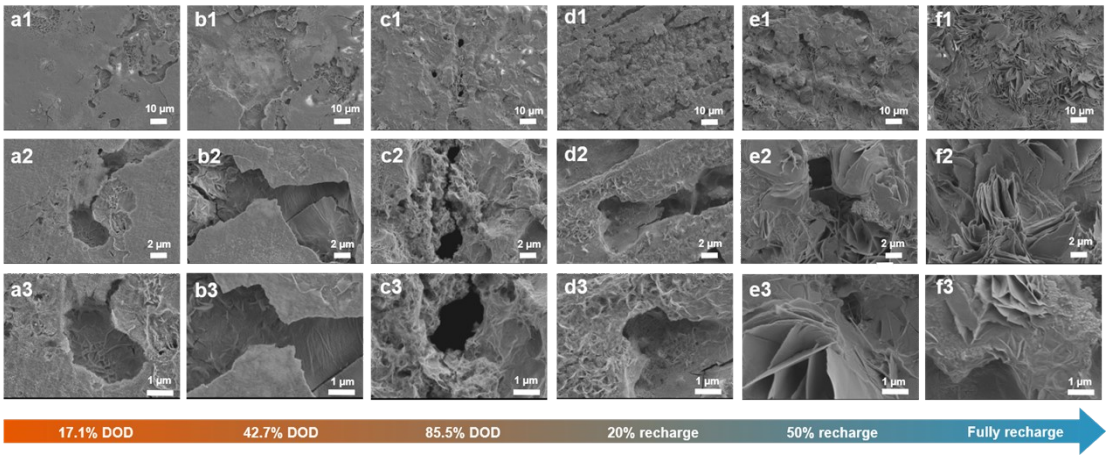

Fig. S12 SEM images of Zn electrodes in pure $Zn(OTf)_2$ electrolyte during 85.5% DOD and fully recharge process.

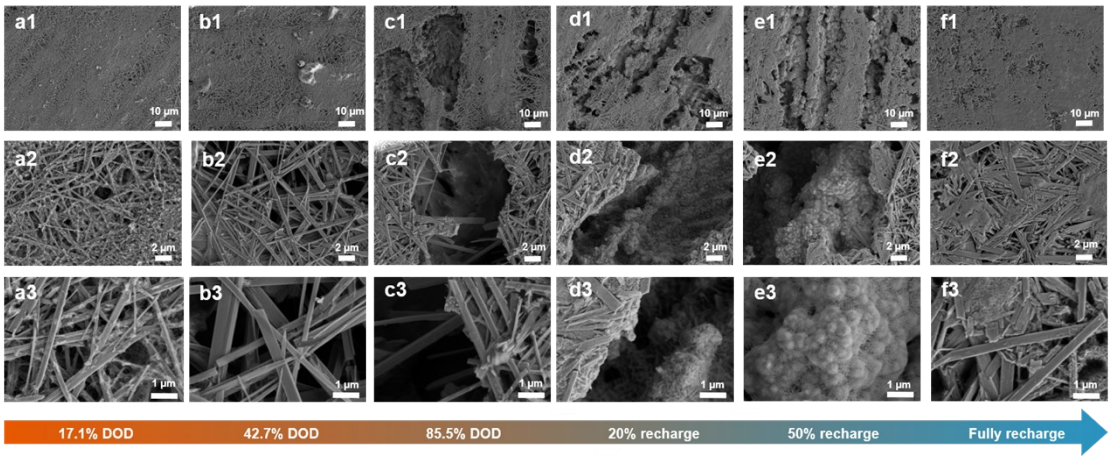

Fig. S13 SEM images of Zn electrodes in AZH/$Zn(OTf)_2$ electrolyte during 85.5% DOD and fully recharge process.

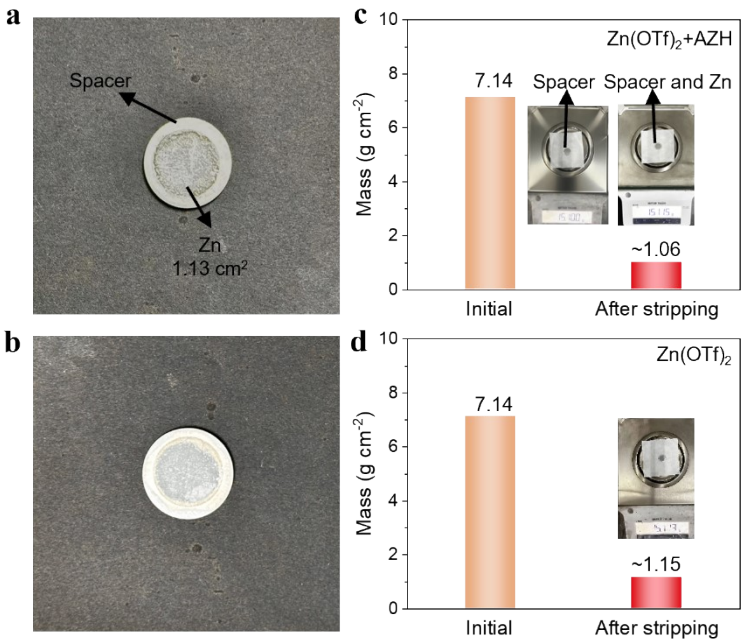

Fig. S14 Optical images of Zn electrodes (10 μm) in (a) AZH/$Zn(OTf)_2$ and (b) pure $Zn(OTf)_2$ electrolytes after stripping for 5 mAh cm^{-2} (85.5% DOD). The mass of Zn electrodes in (c) AZH/$Zn(OTf)_2$ and (d) pure $Zn(OTf)_2$ electrolytes after stripping for 85.5% DOD.

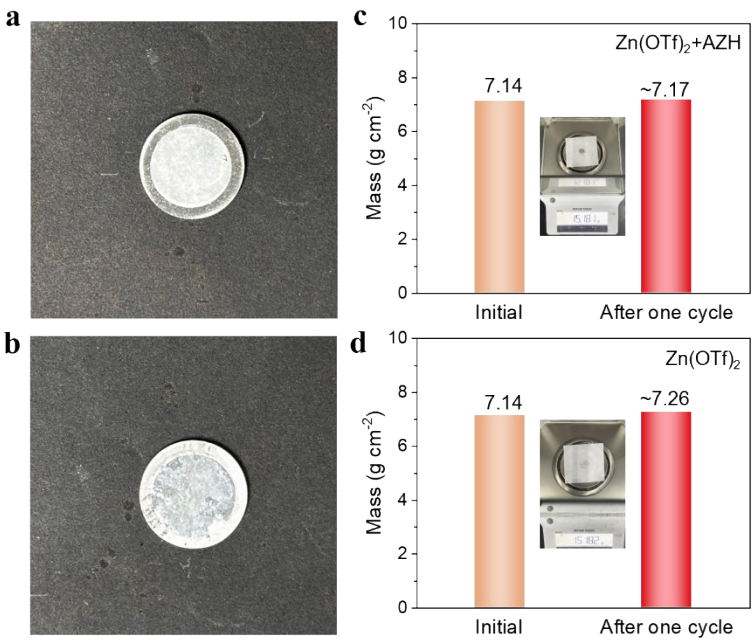

Fig. S15 Optical images of Zn electrodes (10 μm) in (a) AZH/$Zn(OTf)_2$ and (b) pure $Zn(OTf)_2$ electrolytes after one high-DOD (85.5%) cycle. The mass of Zn electrodes in (c) AZH/$Zn(OTf)_2$ and (d) pure $Zn(OTf)_2$ electrolytes after the high-DOD cycle.

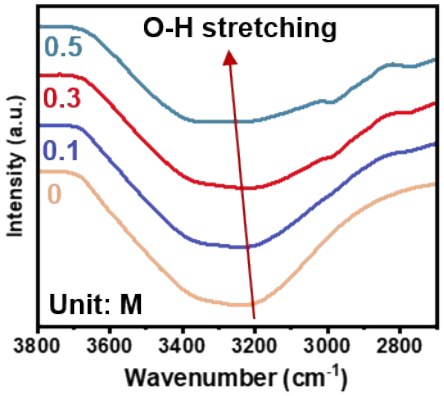

Fig. S16 Fourier transform infrared spectroscopy (FTIR) spectra of O-H stretching for different electrolytes (2 M $Zn(OTf)_2$ with different amount of AZH).

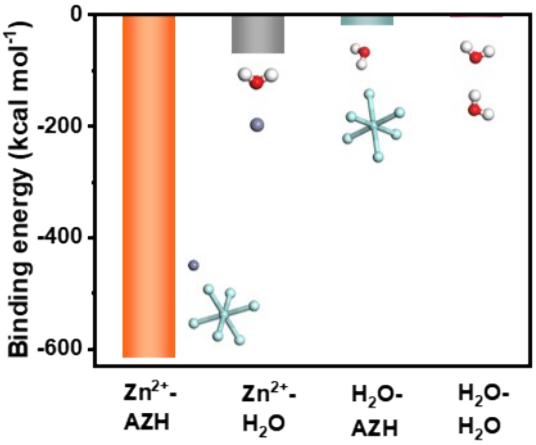

Fig. S17 Binding energies between different molecules.

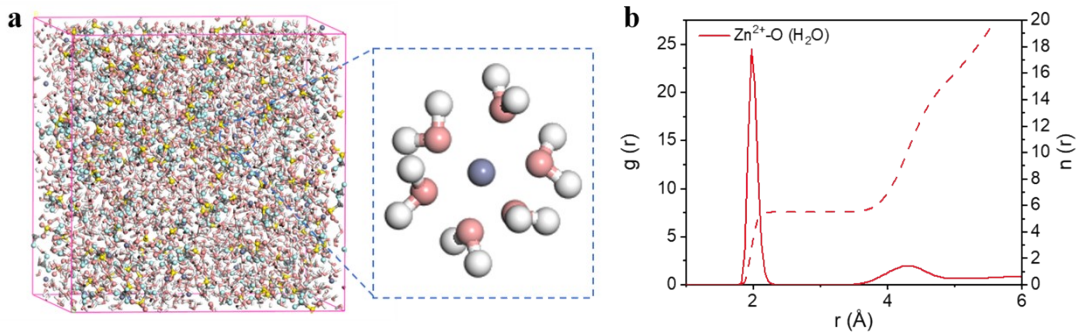

Fig. S18 (a) 3D snapshot of pure $Zn(OTf)_2$ electrolyte obtained from molecular dynamics (MD) simulations and the corresponding Zn^{2+} solvation structure. (b) The radial distribution function (RDF) for Zn^{2+}-O (H_2O) calculated from the MD simulations.

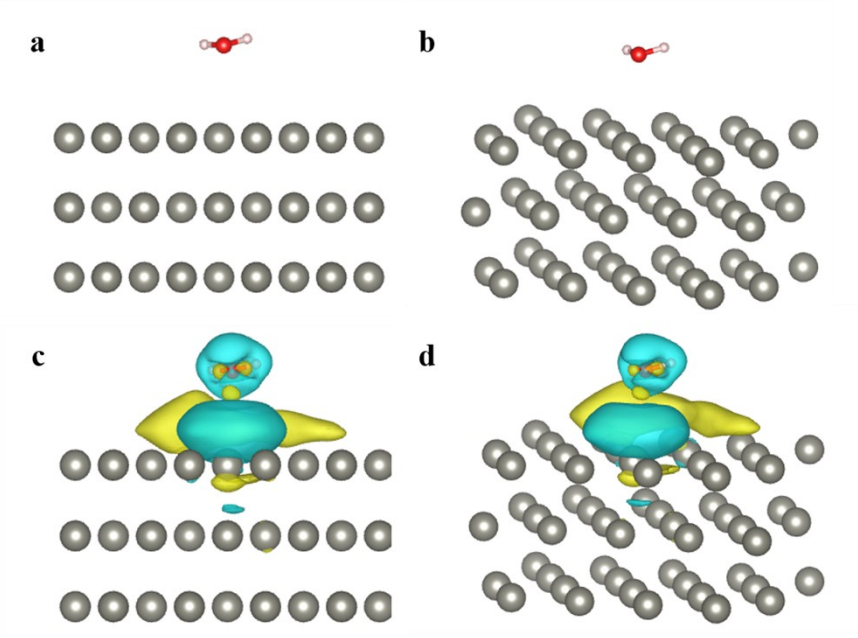

Fig. S19 (a, b) Adsorption models and (c, d) charge density differences of Zn slab with H_2O molecule (noted as Zn-H_2O) at different viewing angles.

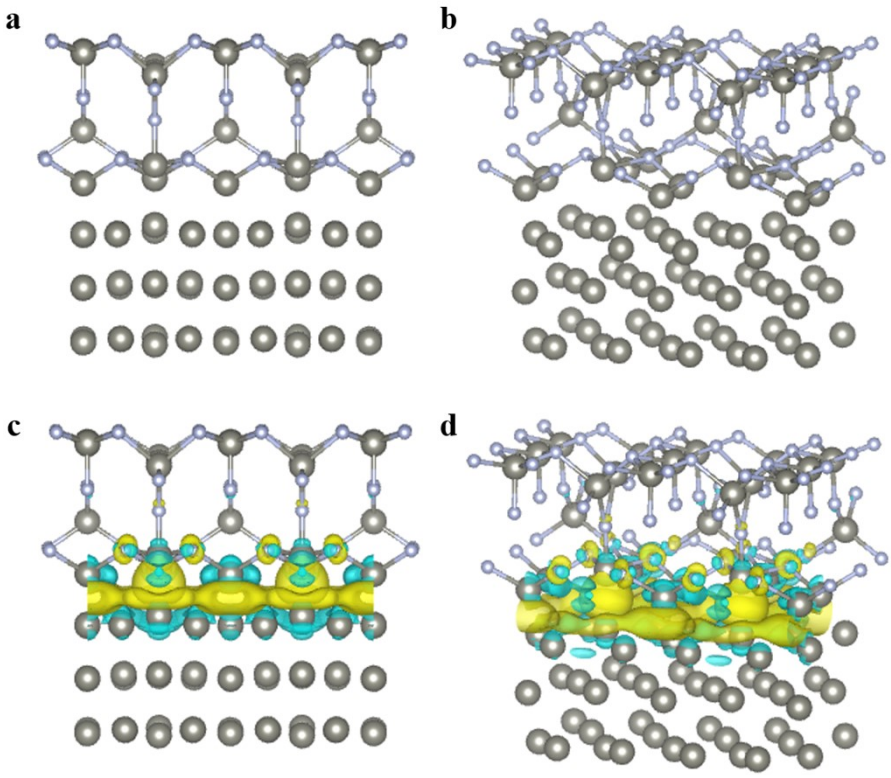

Fig. S20 (a, b) Adsorption models and (c, d) charge density differences of Zn slab with ZnF_2 (noted as Zn-ZnF_2) at different viewing angles.

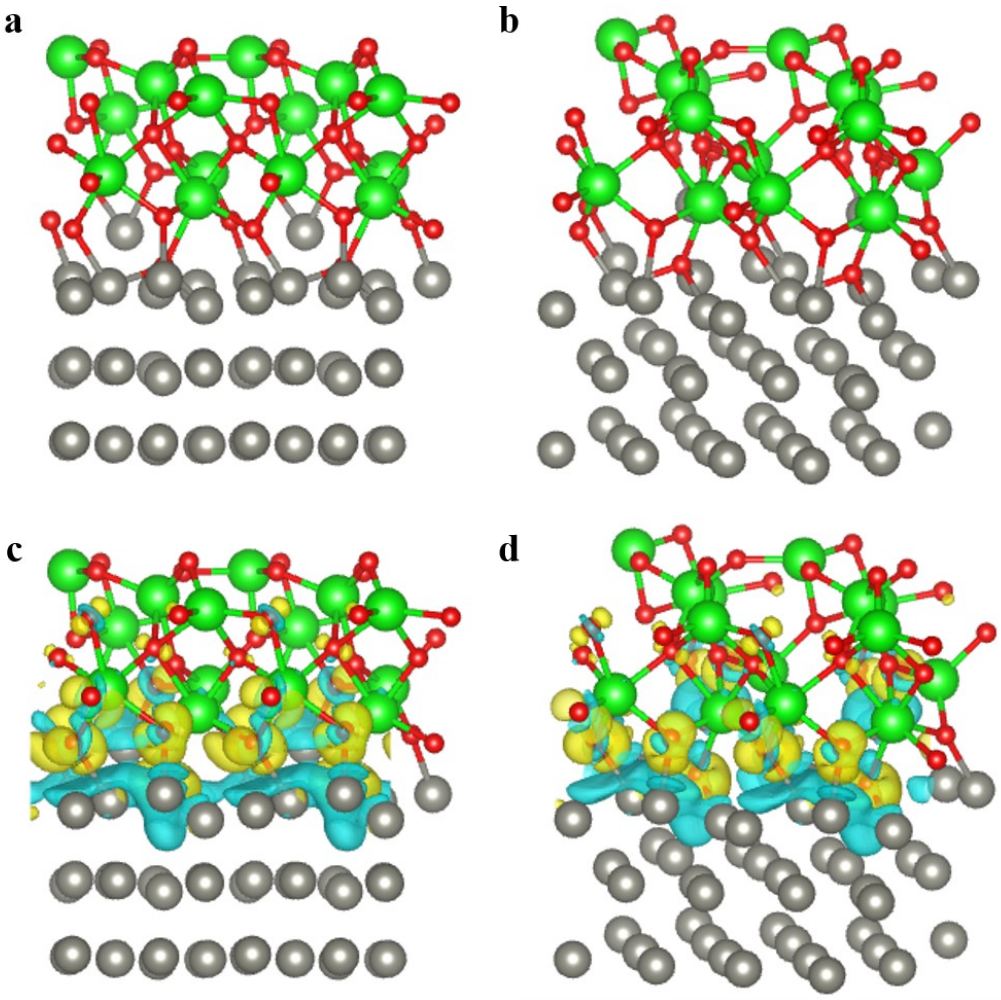

Fig. S21 (a, b) Adsorption models and (c, d) charge density differences of Zn slab with ZrO_2 (noted as Zn-ZrO_2) at different viewing angles.

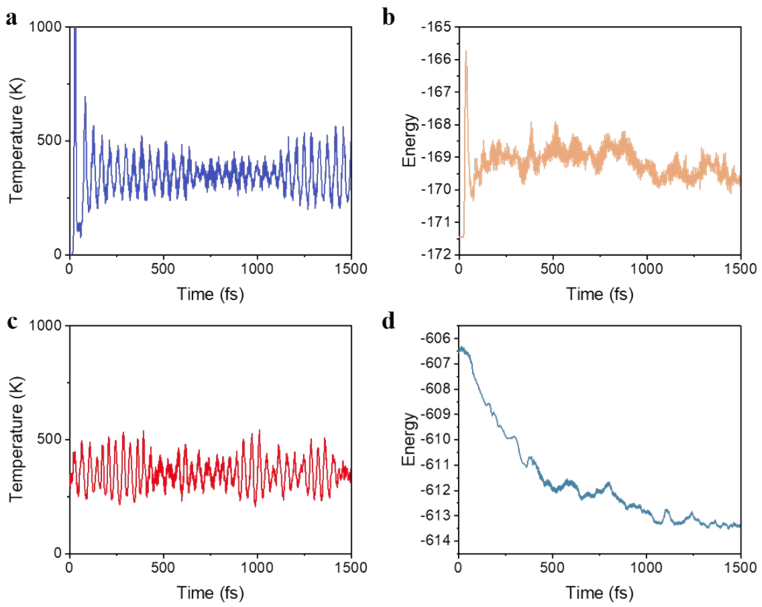

Fig. S22 Temperature control and energy variation in ab initio molecular dynamics (AIMD) simulations of (a, b) pure $Zn(OTf)_2$ and (c, d) AZH/$Zn(OTf)_2$ electrolytes.

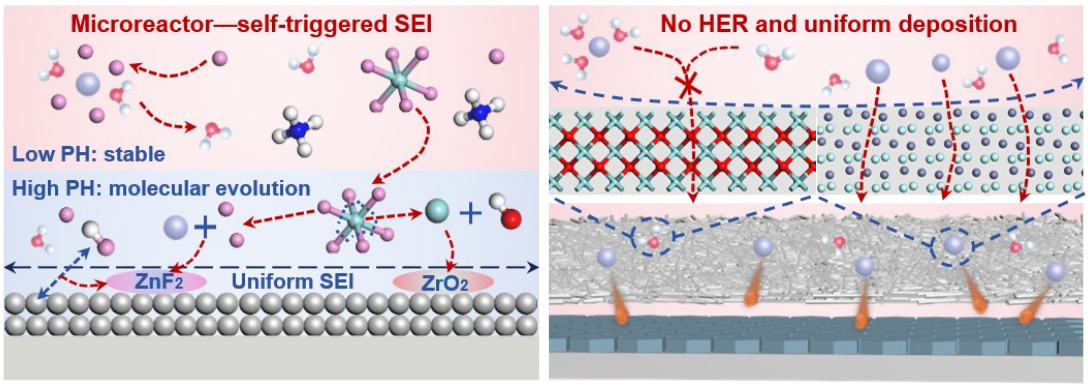

Fig. S23 The interfacial models of Zn anode in AZH/$Zn(OTf)_2$ electrolyte.

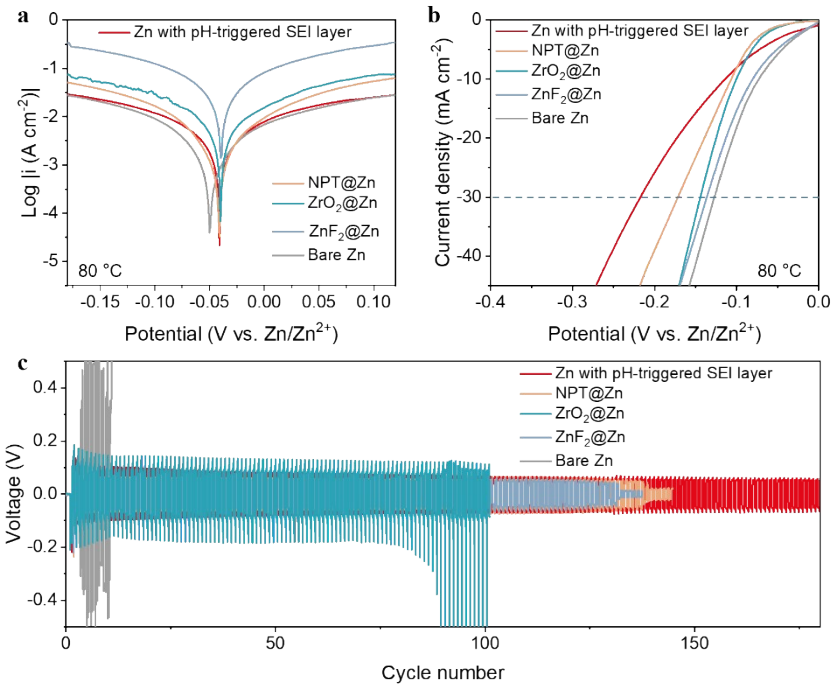

Fig. S24 (a) Corrosion and (b) HER curves of different Zn electrodes at 80 °C. (c) The cycling performance of different symmetrical cells at 20 mA cm^{-2}/5 mAh cm^{-2} (85.5% DOD) under 80 °C.

The Zn electrodes with single ZnF_2 (ZnF_2@Zn), single ZrO_2 (ZrO_2@Zn) and non-pH-triggered ZrO_2/ZnF_2 (NPT@Zn) protective layers are assembled in coin cells to evaluate the roles of fluoride, zirconium, and pH triggering.

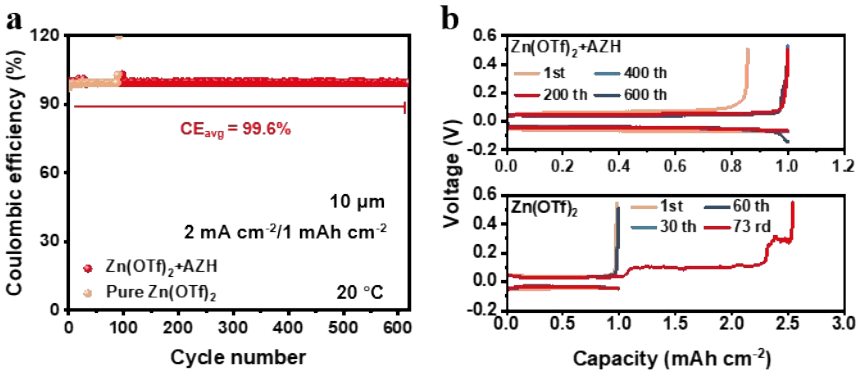

Fig. S25 (a) Coulombic efficiency (CE) measurements of Zn//Cu cells in different electrolytes. (b) Voltage *vs.* capacity curves of Zn//Cu cells at different cycles.

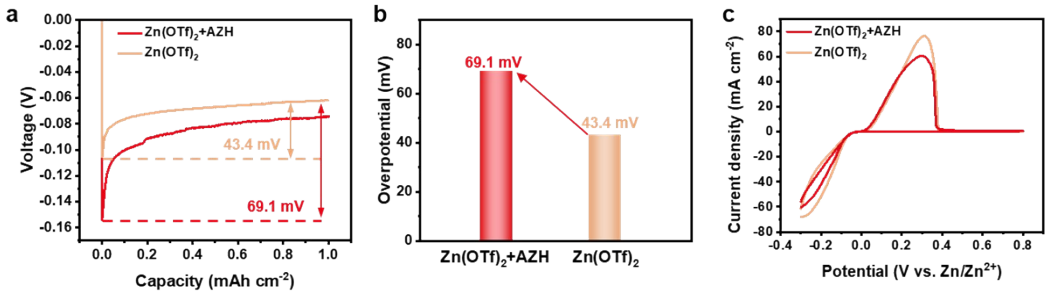

Fig. S26 (a) Voltage-time curves for Zn electrodes deposited at 2 mA cm^{-2} in AZH/$Zn(OTf)_2$ and pure $Zn(OTf)_2$ electrolytes. (b) Zn nucleation overpotentials in different electrolytes. (c) Cyclic voltammetry (CV) curves for Zn//Cu cells in AZH/$Zn(OTf)_2$ and pure $Zn(OTf)_2$ electrolytes.

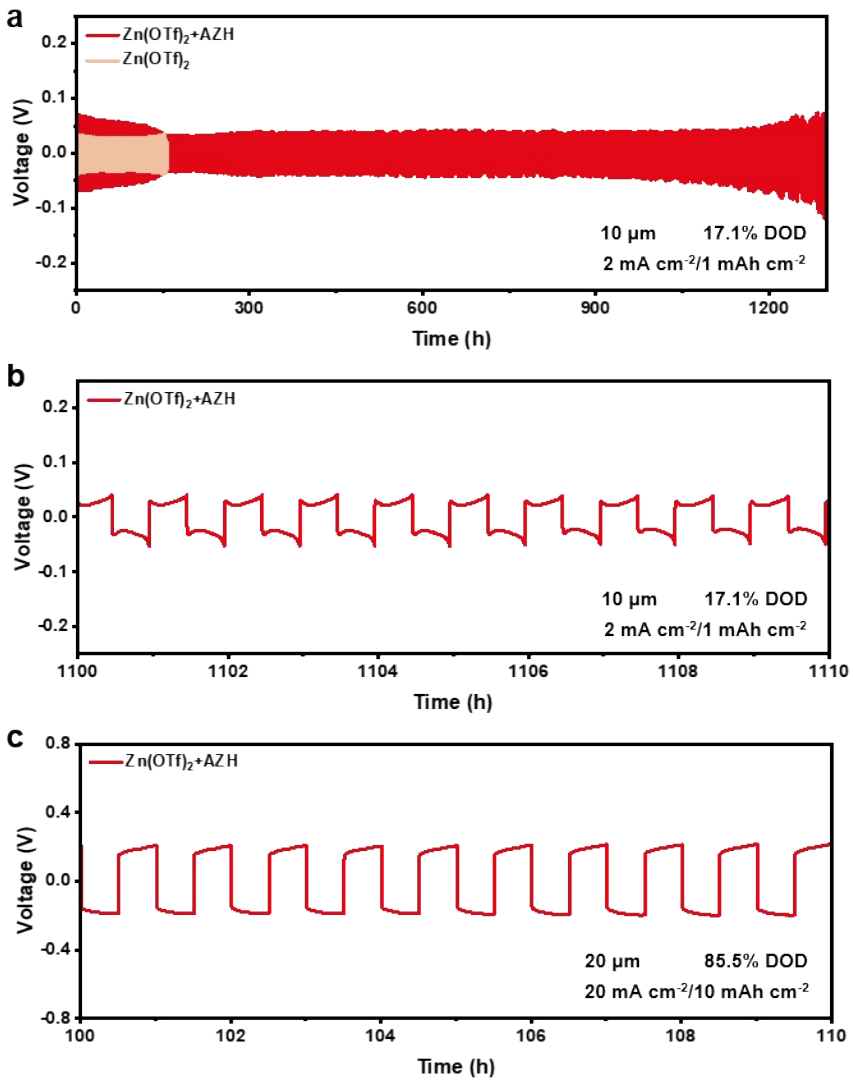

Fig. S27 (a) The cycling performance of Zn//Zn cells at 2 mA cm^{-2}/1 mAh cm^{-2} (17.1% DOD). The magnified voltage profiles of the symmetrical cells at (b) 2 mA cm^{-2}/1 mAh cm^{-2} (17.1% DOD) and (c) 20 mA cm^{-2}/10 mAh cm^{-2} (85.5% DOD).

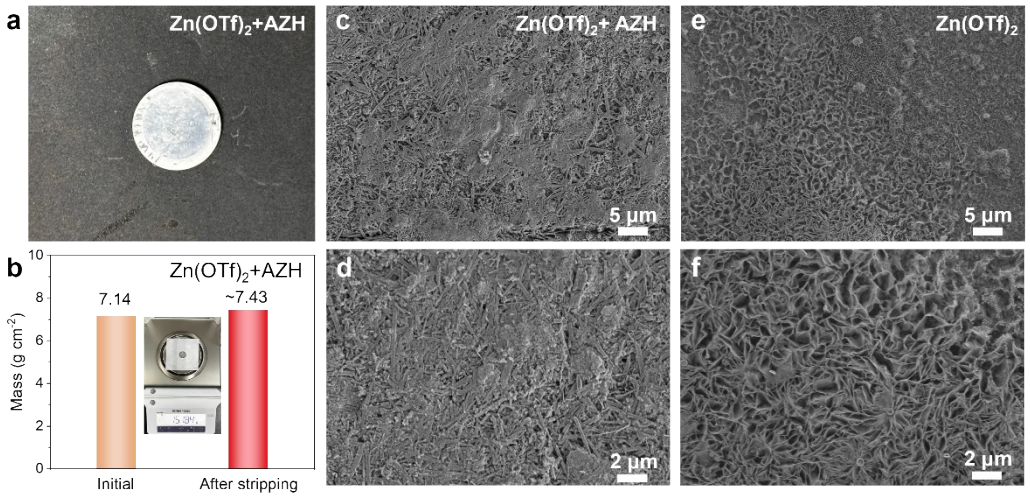

Fig. S28 (a) Optical image and (b) the mass of Zn electrode in AZH/$Zn(OTf)_2$ electrolyte after cycling test at 85.5% DOD. SEM images of Zn electrodes in (c, d) AZH/$Zn(OTf)_2$ and (e, f) pure $Zn(OTf)_2$ electrolytes after the cycling tests.

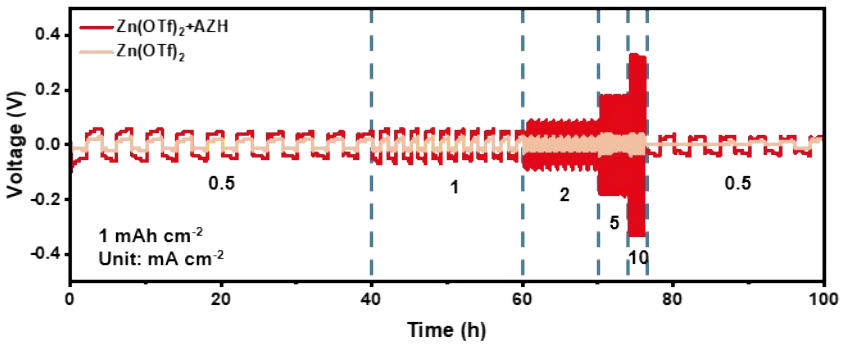

Fig. S29 Rate performance of Zn electrodes in AZH/$Zn(OTf)_2$ and pure $Zn(OTf)_2$ electrolytes.

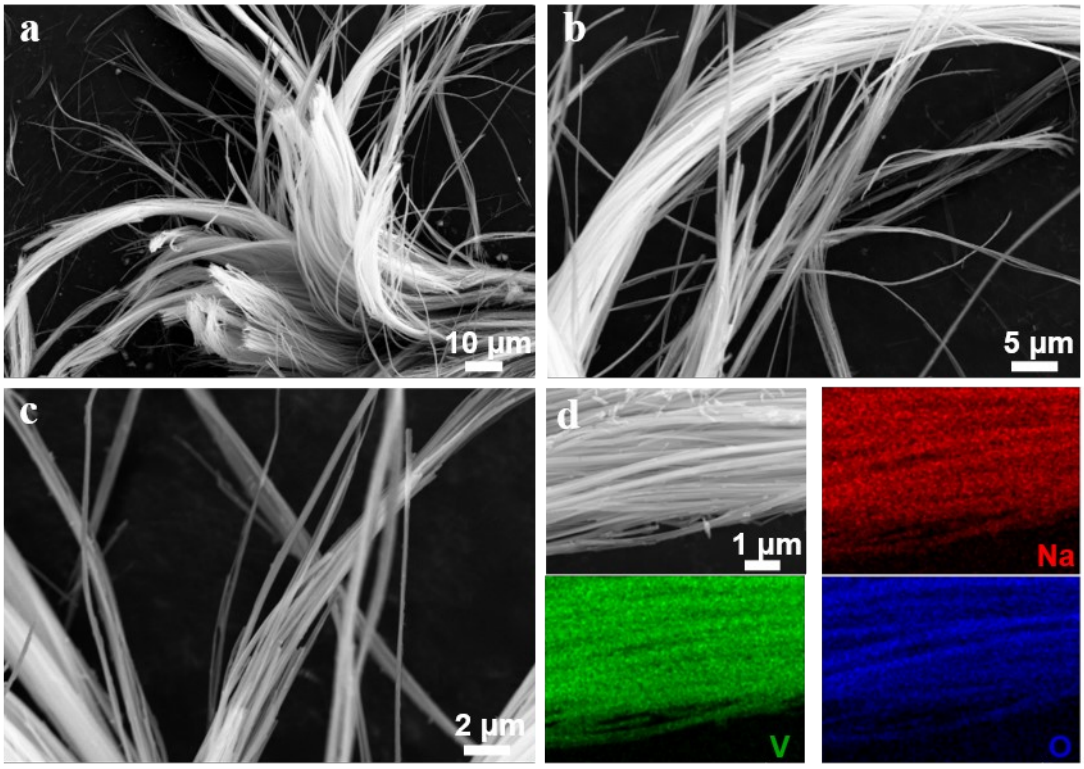

Fig. S30 (a-c) SEM images of the prepared $Na_2V_6O_{16}$ $1.63H_2O$ (NVO) nanowires. (d) SEM image and the corresponding energy dispersive X-ray spectroscopy (EDX) mapping of NVO materials.

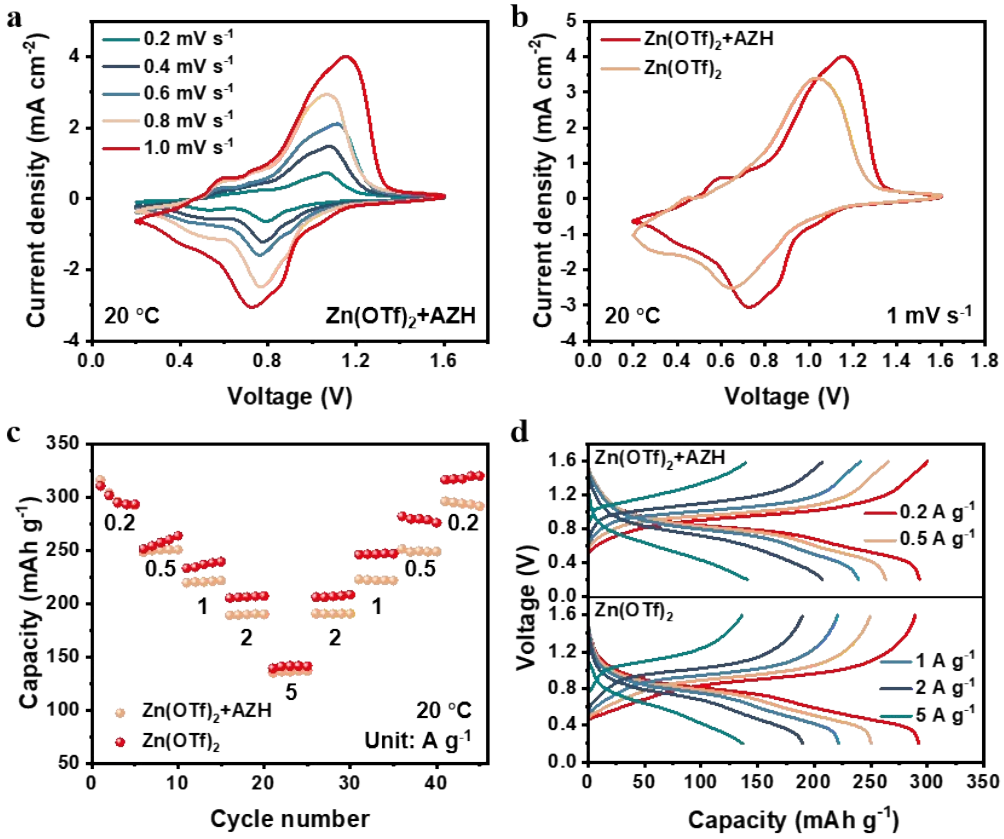

Fig. S31 (a) CV curves of Zn-ion batteries (ZIBs) in AZH/$Zn(OTf)_2$ electrolyte with different scan rates from 0.2 to 1 mV s^{-1}. (b) CV curves of ZIBs in different electrolytes at a scan rate of 1 mV s^{-1}. (c) Rate performance and (d) the corresponding galvanostatic charge/discharge (GCD) curves of ZIBs at various current densities.

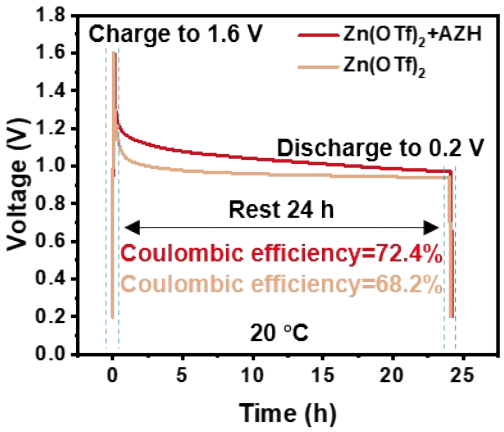

Fig. S32 Capacity retention of ZIBs after charging to 1.6 V, resting for 24 h, and discharging to 0.2 V at 20 °C.

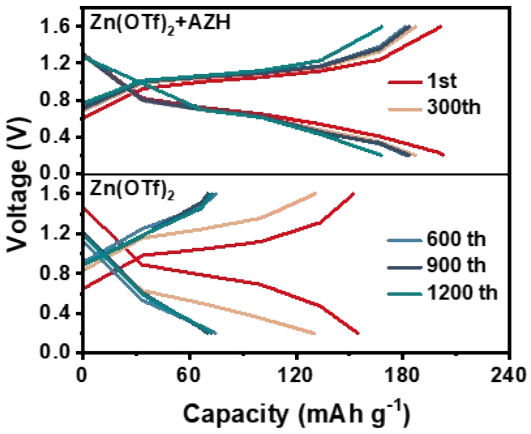

Fig. S33 Voltage-capacity curves of ZIBs at different cycle numbers.

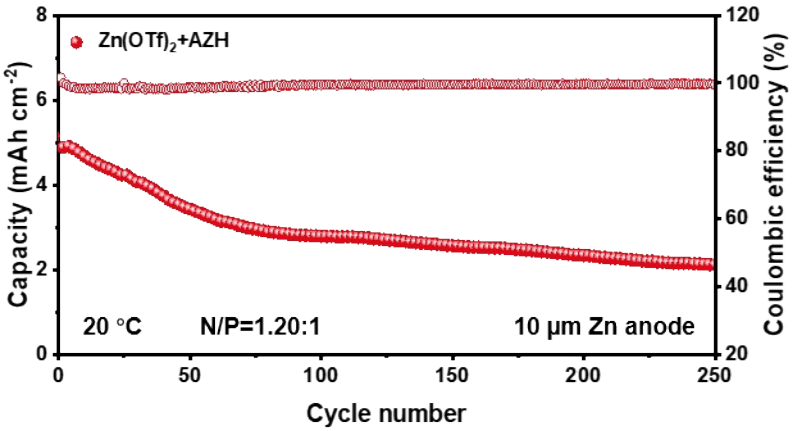

Fig. S34 Cycling performance of ZIB in AZH/$Zn(OTf)_2$ electrolyte with a low N/P ratio (1.20:1) at 20 °C.

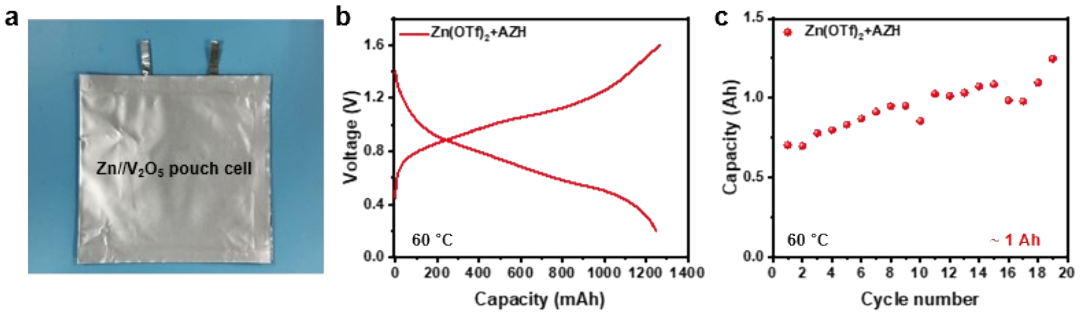

Fig. S35 (a) Optical image of a Zn//V_2O_5 pouch cell with AZH/$Zn(OTf)_2$ electrolyte. (b) GCD curve and (c) cycling performance of the pouch cell at 60 °C.

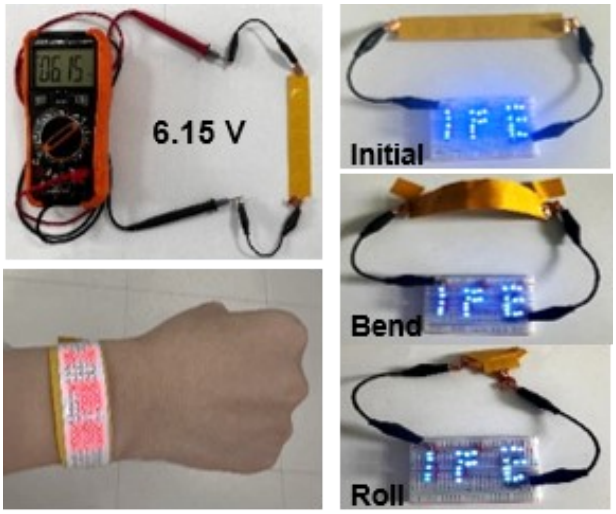

Fig. S36 Optical images of LED flexible screens and arrays powered by the flexible batteries.

Table S1 Comparison of the cycling performance of Zn electrodes in AZH/$Zn(OTf)_2$ electrolyte with recently reported Zn electrodes based on conventional HER suppression strategies at high temperatures**.**

Research	Temperature (°C)	Current density (mA cm^{-2})	Cycling capacity (mAh cm^{-2})	Cumulative capacity (mAh cm^{-2})	Depth of discharge (DOD, %)	Ref.
$Zn(OTf)_2$+ AZH	**20**	**20**	**10**	**2000**	**85.5**	**Our work**
	60	**20**	**5**	**1300**	**85.5**	
	80	**20**	**5**	**900**	**85.5**	
ILEE	60	0.1	0.1	47.5	0.17	Adv. Mater. 2025 [8]
RGSH	70	0.25	0.25	50	4.27	Angew. Chem., Int. Ed. 2025 [9]
THFA	60	1	0.5	75	1.71	Adv. Funct. Mater. 2024 [10]
$ZnCl_2$+SF	60	2	2	200	3.42	Angew. Chem., Int. Ed. 2025 [11]
SSE25	80	0.5	0.5	32.5	0.85	Adv. Energy Mater. 2024 [12]
TSAE	75	1	1	200	2.14	Adv. Mater. 2024 [13]
HZLE-1	80	1	1	225	17.1	Energy Environ. Sci. 2025 [14]
ZFC	60	1	1	140	1.71	Adv. Funct. Mater. 2025 [15]
	60	0.5	0.25	175	0.43	
MAA30	60	1	0.5	150	1.71	Energy Storage Mater. 2025 [16]
PSPZ	60	0.1	0.1	20	1.71	Adv. Funct. Mater. 2024 [17]
	80	0.3	0.3	30	5.13	
DEE	80	/	0.1	87.75	0.17	Energy Environ. Sci. 2024 [18]
BE-DX	60	0.5	0.25	250	4.27	Energy Storage Mater. 2024 [19]

Table S2 The important cell details for the full ZIBs**.**

Full ZIBs	Zn anode (μm)	Separator	Electrolyte (μL)	Cathode (mg)	E to S ratio (μL mg^{-1})	Capacity (mAh)	E to C ratio (mL Ah^{-1})
Figs. 6a-c (coin cell)	10	GF-A, Whatman	80	1.7 (NVO)	47.1	0.35	228.6
Fig. 6d (coin cell)	10	GF-A, Whatman	80	15 (V_2O_5)	5.3	4.71	17.0
Fig. 6e (coin cell)	20	GF-A, Whatman	90	20 (V_2O_5)	4.5	7.89	11.4
Fig. S30 (pouch cell)	20	Glass fiber and nylon membrane	13000	~3800 (V_2O_5)	3.4	1247.06	10.4

The NVO coin cell demonstrates a high electrolyte/capacity (E/C) ratio of 228.6 mL Ah^{-1}, which is far from practical levels. This value can be reduced by decreasing the electrolyte amount and increasing the cathode loading for practical usage.

Table S3 Comparison of the energy density of recently reported ZIBs (based on the whole mass of both active electrodes).

Research	Mass loading of cathode (mg cm^{-2})	Zn anode thickness (μm)	Mass loading of Zn anode (mg cm^{-2})	Areal capacity (mAh cm^{-2})	Energy density (Wh kg^{-1})	Ref.
V_2O_5	**20**	**20**	**14.3**	**7.89**	**150.4**	**Our work**
MnO_2	0.7	100	71.4	0.15	0.6	Adv. Funct. Mater. 2022 [20]
MnO_2@C	0.8	100	71.4	0.2	0.9	Nat. Commun. 2023 [21]
ZnVO	11	10	7.14	3.2	105	Adv. Mater. 2023 [22]
VOH	16.6	20	14.3	5.38	31.4 (full cell)	Angew. Chem. Int. Ed. 2025 [11]
$V_2O_5 \cdot nH_2O$	2.5	/	/	0.93	90	Adv. Mater. 2018 [23]
$Zn_{0.25}V_2O_5 \cdot nH_2O$	6.7	10	7.14	1.4	26 (full cell)	Adv. Mater. 2024 [24]
TP-Se	2.2	100	71.4	0.7	18.6	Chem 2022 [25]
I_2	15	30	21.4	3.0	134	Energy Environ. Sci. 2022 [26]
NVO	9.3	10	7.14	2.8	86.1	Nat. Commun. 2023 [27]

References

1 Y. Gao, N. Yang, F. Bu, Q. Cao, J. Pu, Y. Wang, T. Meng, J. Chen, W. Zhao and C. Guan, *Energy Environ. Sci.*, 2024, **17**, 1894-1903.

2 G. Kresse and J. Furthmüller, *Comput. Mater. Sci.*, 1996, **6**, 15-50.

3 J. Perdew, K. Burke and M. Ernzerhof, *Phys. Rev. Lett.*, 1996, **77**, 3865.

4 S. Grimme, J. Antony, S. Ehrlich and H. Krieg, *J. Chem. Phys.*, 2010, **132**, 154104.

5 V. Wang, N. Xu, J. Liu, G. Tang and W. Geng, *Comput. Phys. Commun.*, 2021, **267**, 108033.

6 S. Nosé, *Comput. J. Chem. Phys.*, 1984, **81**, 511.

7 W. Hoover, *Phys. Rev. A.*, 1985, **31**, 1695.

8 M. Qiu, Y. Xin, Y. Liang, Y. Liu, J. Chen, J. Li, P. Sun, H. J. Fan and W. Mai, *Adv. Mater.*, 2025, **37**, 2418947.

9 Y. Chen, S. Zhou, J. Li, X. Zhang, C. Zhou, X. Shi, C. Zhang, G. Fang, S. Liang, Z. Su and A. Pan, *Angew. Chem., Int. Ed.*, 2025, **64**, e202423252.

10 Y. Qiu, X. Zheng, R. Zhang, Q. Lin, M. Li, J. Luo, S. Yang, Z. Liu, Q. Wang, Y. Yu and C. Yang, *Adv. Funct. Mater.*, 2024, **34**, 2310825.

11 L. Zhang, Y. Han, Y. Geng, H. Zhang, H. Liu, Y. He, Z. Yan and Z. Zhu, *Angew. Chem., Int. Ed.*, 2025, **64**, e202500434.

12 X. Yun, Y. Chen, H. Gao, D. Lu, L. Zuo, P. Gao, G. Zhou, C. Zheng and P. Xiao, *Adv. Energy Mater.*, 2024, **14**, 2304341.

13 G. Qu, H. Wei, S. Zhao, Y. Yang, X. Zhang, G. Chen, Z. Liu, H. Li and C. Han, *Adv. Mater.*, 2024, **36**, 2400370.

14 M. Yang, X. Zou, M. Wu, J. Yu, X. Ma, Y. Hu and F. Yan, *Energy Environ. Sci.*, 2025, **18**, 3365-3375.

15 C. Zhuang, S. Zhang, Z. G. Yu, J. Yang, Y. Sun, H. Wen, H. Wen, H. Li, B. Yin and T. Ma, *Adv. Funct. Mater.*, 2025, **35**, 2419351.

16 N. Yu, S. Lin, S. Zhou, Y. Li, J. Li, Q. Zeng, L. Chen, L. Wang, K. Guo, X. Wang and Y. Li, *Energy Storage Mater.*, 2025, **80**, 104398.

17 Y. Li, X. Yang, Y. He, F. Li, K. Ouyang, D. Ma, J. Feng, J. Huang, J. Zhao, M. Yang, Y. Wang, Y. Xie, H. Mi and P. Zhang, *Adv. Funct. Mater.*, 2024, **34**, 2307736.

18 X. Bai, M. Sun, J. Yang, B. Deng, K. Yang, B. Huang, W. Hu and X. Pu, *Energy Environ. Sci.*, 2024, **17**, 7330-7341.

19 Y. Xiao, D. Han, B. Zhang, C. Cui, Z. Li, D. Fan, Y. Liu, Q. Li, F. Li, K. Xie, J. Wen, Z. Weng and Q.-H. Yang, *Energy Storage Mater.*, 2024, **72**, 103693.

20 Q. Cao, Z. Pan, Y. Gao, J. Pu, G. Fu, G. Cheng and C. Guan, *Adv. Funct. Mater.*, 2022, **32**, 2205771.

21 Q. Cao, Y. Gao, J. Pu, X. Zhao, Y. Wan g, J. Chen and C. Guan, *Nat. Commun.*, 2023, **14**, 641.

22 G. Liang, Z. Tang, B. Han, J. Zhu, A. Chen, Q. Li, Z. Chen, Z. Huang, X. Li, Q. Yang and C. Zhi, *Adv. Mater.*, 2023, **35**, 2210051.

23 M. Yan, P. He, Y. Chen, S. Wang, Q. Wei, K. Zhao, X. Xu, Q. An, Y. Shuang, Y. Shao, K. T. Mueller, L. Mai, J. Liu and J. Yang, *Adv. Mater.*, 2018, **30**, 1703725.

24 Y. Shang, V. Kundi, I. Pal, H. N. Kim, H. Zhong, P. Kumar and D. Kundu, *Adv. Mater.*, 2024, **36**, 2309212.

25 Z. Chen, H. Cui, Y. Hou, X. Wang, X. Jin, A. Chen, Q. Yang, D. Wang, Z. Huang and C. Zhi, *Chem*, 2022, **8**, 2204-2216.

26 G. Liang, J. Zhu, B. Yan, Q. Li, A. Chen, Z. Chen, X. Wang, B. Xiong, J. Fan, J. Xu and C. Zhi, *Energy Environ. Sci.*, 2022, **15**, 1086-1096.

27 Y. Wang, Z. Wang, W. K. Pang, W. Lie, J. A. Yuwono, G. Liang, S. Liu, A. M. D. Angelo, J. Deng, Y. Fan, K. Davey, B. Li and Z. Guo, *Nat. Commun.*, 2023, **14**, 2720.